PHILOSOPHICAL TRANSACTIONS OF THE ROYAL SOCIETY A MATHEMATICAL, PHYSICAL & ENGINEERING SCIENCES

Spatio–temporal dynamics of acoustic cavitation bubble clouds

U. Parlitz, R. Mettin, S. Luther, I. Akhatov, M. Voss and W. Lauterborn

Phil. Trans. R. Soc. Lond. A 1999 **357**, 313-334
doi: 10.1098/rsta.1999.0329

THE ROYAL SOCIETY

Spatio-temporal dynamics of acoustic cavitation bubble clouds

By U. Parlitz[1], R. Mettin[1], S. Luther[1], I. Akhatov[2], M. Voss[1] and W. Lauterborn[1]

[1]*Drittes Physikalisches Institut, Universität Göttingen, Bürgerstr. 42–44, 37073 Göttingen, Germany*

[2]*Ufa Branch of Russian Academy of Sciences and Bashkir University, K. Marx Str. 6, Ufa, 450000, Russia*

Bubble clouds forming in an extended volume of liquid in acoustic cavitation show a slowly varying filamentary structure, whose origin is still not completely understood. Experimental observations are reported that provide some characteristics of the phenomenon, such as bubble distributions and sound-field measurements. A discussion of relevant physical interactions in bubbly liquids is comprised of wave dynamics, Bjerknes and drag forces, nucleation and coalescence. For describing the structure formation process, continuum and particle approaches are employed. In the framework of the continuum model it is shown that homogeneous bubble distributions are unstable, and regions with high bubble concentration emerge in the course of a self-concentration process. In the particle model, all bubbles are treated as interacting objects that move in the liquid. This approach is complementary to the continuum model. It allows the inclusion of some particular features, for instance Bjerknes forces based on nonlinear bubble oscillations. Both models are discussed and results are compared with experimentally observed patterns.

Keywords: structure formation; chaotic dynamics; Bjerknes forces; wave equation; particle model

1. Introduction

The onset of acoustic cavitation is usually defined as the inception of bubbles in an otherwise uniform acoustically irradiated liquid. The threshold amplitude of sound pressure for this process depends on many parameters like the frequency of the sound, type of liquid, amount of dissolved gas and impurities, or static pressure. However, a robust almost universal phenomenon shown by the once generated acoustic cavitation bubbles is the formation of structures. The spatial distribution of bubbles in the observed clouds is usually not homogeneous. Instead, filamentary patterns of streaming bubbles emerge like that shown in figure 1.

The generic emergence of bubble structures in high-intensity sound fields is visually striking, and also the study of such inhomogeneous spatial bubble distributions is relevant for many technical and chemical applications of ultrasound in liquids (Mason, this issue). Nevertheless, a detailed understanding of the mechanisms leading to this self-organizing phenomenon has only begun recently. In this paper, we would like to acquaint the reader with experimental results, physical background and the complexity of the phenomenon, and highlight the research pathway undertaken to gain a deeper understanding.

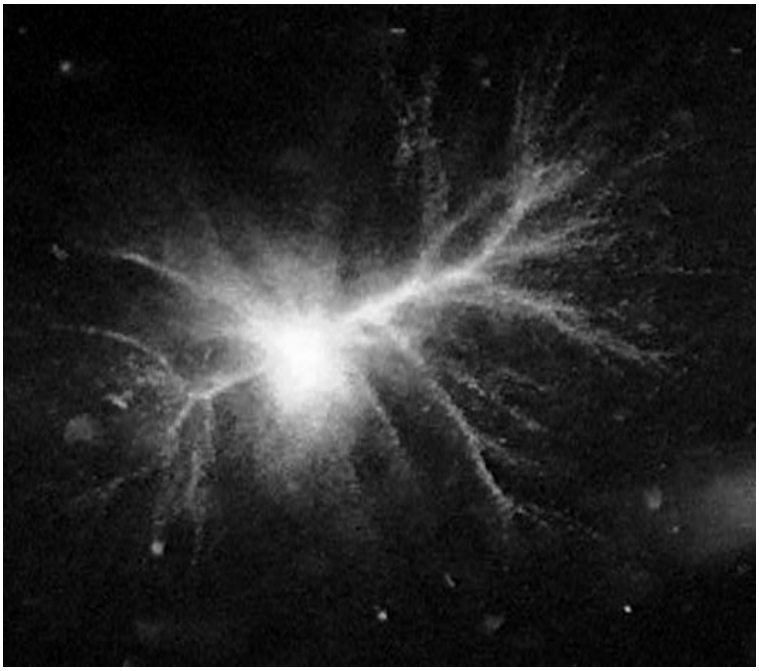

Figure 1. Structure of streaming bubbles ('acoustic Lichtenberg figure') emerging in a standing acoustic wave. Bright regions correspond to light scattered by the bubbles (2 ms exposure time).

A complete consideration of spatio-temporal dynamics of acoustically driven multi-bubble systems includes several time-scales and spatial scales. The slowest time-scale is specified by the drift of the filaments, or rearrangement time of the structures, which is in the range of 0.1 to several seconds. The relaxation time of bubble motion gives an intermediate time-scale in the range of 10^{-2}–10^{-3} s. A fast scale is defined by the period T of the acoustic driving, $T \approx 10^{-4}$–10^{-5} s. Even faster are effects connected with a strong bubble collapse (10^{-9} s) or accompanying light emission (10^{-10} s). In our experiments, the macroscopic spatial scale is characterized by the acoustic wavelength and the boundary conditions that amount to centimetres. A mesoscopic scale is given by typical distances between bubbles and ranges between 0.1 and 1 mm, and bubble radii define a microscopic spatial scale of about 10^{-5} m. Further sub-microscales are relevant in connection with strong collapse and light emission (below 1 μm). On these smallest scales we find the cavitation nuclei and microbubbles, not visible in the structures but responsible for cavitation in the considered pressure regime.

The process we are interested in has temporal as well as spatial structure formation aspects. The temporal aspect is given by the occurrence of subharmonic and low-dimensional chaotic response, e.g. due to a period-doubling cascade. This is detectable for individual bubble oscillations and for the averaged sound emission. The spatial aspect is manifested in the evolution of dendritic filamentary structures consisting of hundreds or thousands of individual cavitation bubbles. The evolving pattern, visible to the naked eye, is small compared to the (wave-) length of macroscopic disturbances but large compared to the inter-bubble distance. It is structurally

stable on time-scales large compared to the bubble oscillations. Thus one may ask: how do the individual microscopic oscillations and motions of the cavitation bubbles evolve into a macroscopic and coherent structure, and how does the structure influence the individual bubbles?

2. Experimental observations

The structures we are interested in can best be observed in standing pressure waves. A closer examination of examples like that shown in figure 1 reveals roughly the following.

Most of the bubbles are generated at impurities that reside at boundaries like the vessel walls or the hydrophone. Such locations will be called 'nucleation sites' in the following. From the nucleation sites, the bubbles move in the direction of a pressure antinode, where a cluster of bubbles occurs. Note that, in general, the bubbles are so small when created at the nucleation sites that they appear 'invisible'. During their motion to the central cluster, however, they reach a region of higher pressure amplitude that lets them oscillate to a visible maximum size. The locations where the bubbles become visible for the first time will be called 'emerging sites' in order to avoid misinterpretation of experimental observations. The emerging sites are located at approximately the same distance from the pressure antinode. Because all the bubbles that can be traced from an emerging site follow almost identical paths, a 'streamer' (Flynn 1964; Neppiras 1980) becomes visible. The streams of bubbles join and finally unite in the cluster. The whole structures resemble certain electrical discharge or lightning patterns, and we therefore call them 'acoustic Lichtenberg figures' (ALFs) in the following, in analogy to the well-known electrical Lichtenberg figures†. These patterns are considered 'stable', because in experimental observations (Lauterborn *et al*. 1993, 1997) the structures, including the fingers of moving bubbles, stay roughly the same on a time-scale of fractions of a second up to seconds, before any subsequent visible changes occur. This is much longer than the acoustic field period and about what we estimate to be the travel time of a bubble to the centre. While in a stable pattern, many bubbles appear one after the other at about the same position in space and subsequently take almost identical paths to a cluster.

Only at very low pressure amplitudes in fresh tap water containing many submerged bubbles will the instreaming bubbles form a larger one that leaves the centre after reaching a certain critical size. In a typical ALF, however, we observe only some kind of 'microbubble mist' leaving the central cluster (visible as a bright halo in the middle of figure 1). This happens despite the prediction that very small bubbles should be attracted towards a pressure antinode. We suspect that the small bubbles in the mist, fragments of the larger bubbles, are weakly attracted to the pressure antinodes such that they may be advected outward by the liquid motion. This observation seems to answer, in part, the questions about mass conservation of the instreaming gas in the bubbles. The motion of liquid might participate in some more aspects of cavitation structures, but it is more difficult to investigate than the bubble motion. Simple methods, like ink drops, indicate that liquid velocities apparently increase by an order of magnitude at the cavitation threshold, and that the streaming near the pressure antinode is much faster than near the container walls.

† Structures without a central cluster are also possible as we will report later on.

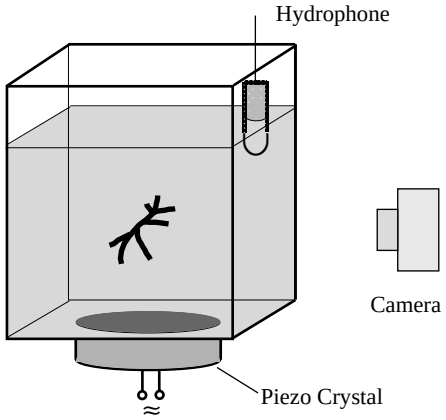

Figure 2. Experimental arrangement for cavitation structure investigations. The water volume is 5 cm × 5 cm × 5 cm.

The arrangement used for the experiments presented in this article is shown in figure 2. The transparent rectangular container is open at the top, and the water fill-height equals the base length to yield an approximately cubic water volume. (Similar results have also been obtained with other geometries like cylindrical or spherical vessels.)

The sound field is generated by a piezoelectric element driven sinusoidally at about 20 kHz. The frequency is adjusted to the (111) mode, and a standing wave occurs with pressure antinode in the middle of the cuvette. The bubble structures are illuminated from the outside, and pictures of the scattered light were taken with a CCD camera. The filaments that can be seen by the naked eye (see figure 1) represent bubble trajectories where single bubbles are not resolved. If snapshots with a shorter exposure time (*ca.* 3 µs) are taken, it becomes apparent that the filaments are only sparsely populated (compare with figure 3). At the same time as the optical observation, the acoustic signal can be measured by using a small hydrophone (Brüel & Kjaer 8103) located near a corner of the cuvette. The hydrophone measures the emissions of the transducer and of all bubbles, each scattering sound waves while oscillating and possibly emitting shock waves at strong collapse. Thus, there are many individual sources contributing to the signal.

In figure 3, we compare acoustic measurements with the observed patterns. Measured time-series $s(t)$ from the hydrophone were taken with a sampling time of $\Delta t =$ 200 ns. A three-dimensional delay embedding (Takens 1980; Sauer *et al*. 1991; Lauterborn & Parlitz 1988; Lauterborn & Holzfuss 1991) $\boldsymbol{x}(t) = (s(t), s(t-\tau), s(t-2\tau))$ of such a time-series with a delay time $\tau = 8\Delta t = 1.6$ µs is given in figure 3*b*. This reconstruction of the dynamics provides strong evidence for the existence of a low-dimensional attractor, at least for the time covered by the time-series (10 000 samples, corresponding to 2 ms). This period of time is small compared to the typical time-scale on which the ALF changes its shape, and we can therefore assume the system (i.e. the bubble configuration and its acoustic coupling) to be stationary. On a longer time-scale (greater than 0.1 s), however, the branches of the ALF move and the bubble distribution changes. This can be seen in figure 3*c*, taken a few seconds after figure 3*a*. Figure 3*d* shows a delay reconstruction of the corresponding time-

series. The shape of the reconstructed attractor differs considerably from that shown in figure 3*b*, and thus the change of the ALF comes with a change of the dynamics of the coupled bubble oscillations and of the sound emission by the oscillating bubbles. Besides acoustic measurements, additional evidence for low-dimensional (i.e. *uni sono*, synchronized) behaviour of the bubbles has been given by optical measurements (scattered-light intensity and high-speed holography). We refer to Ohl *et al.* (this issue).

These observations raise several questions. Why, at least on short time-scales, is the dynamics of the system of hundreds or thousands of coupled bubbles so low dimensional? Are there stages of the evolution of the ALF during which the acoustic signal *cannot* be characterized as low dimensional? What are the dynamical properties of the long-term evolution of the ALF? To address these questions, both acoustic and optical long-term measurements and numerical simulations are needed; they became possible only recently. We suspect that the observed low dimensionality of the dynamics might be a result of synchronization phenomena, in particular chaotic phase synchronization (Rosenblum *et al.* 1996; Parlitz *et al.* 1996). Furthermore, we conjecture that the long-term evolution of the ALF is *not* a low-dimensional phenomenon.

3. Physical interactions in bubbly liquids

In order to develop a theoretical model of the structure-formation process described in the previous section, many physical mechanisms and features have to be considered. In this section, we briefly present those mechanisms that constitute the building blocks of the continuum and particle models to be introduced in the following sections.

(*a*) *Nonlinear spherical-bubble oscillations*

Bubbles that are subject to periodic sound fields with medium- or high-pressure amplitude oscillate strongly nonlinear, including complex shape oscillations (Plesset 1954; Strube 1971; Prosperetti 1977). For simplicity, we assume here that the shape of the bubbles remains spherical and use the model of Keller & Miksis (1980):

$$\left(1-\frac{\dot R}{c}\right)R\ddot R+\tfrac{3}{2}\dot R^2\left(1-\frac{\dot R}{3c}\right)=\left(1+\frac{\dot R}{c}\right)\frac{p_{\rm l}}{\rho}+\frac{R}{\rho c}\frac{{\rm d}p_{\rm l}}{{\rm d}t}, \tag{3.1}$$

$$\left.\begin{aligned} p_{\rm l}&=\left(p_0+\frac{2\sigma}{R_0}\right)\left(\frac{R_0}{R}\right)^{3\kappa}-p_0-\frac{2\sigma}{R}-\frac{4\mu}{R}\dot R-p_{\rm a}(t),\\ p_{\rm a}(t)&=P_{\rm a}\cos(\omega t),\end{aligned}\right\} \tag{3.2}$$

for air bubbles in water at 20 °C with the polytropic exponent $\kappa=1.4$, surface tension $\sigma=0.0725\,{\rm N\,m^{-1}}$, liquid density $\rho=998\,{\rm kg\,m^{-3}}$, viscosity $\mu=0.001\,{\rm Ns\,m^{-2}}$, ambient pressure $p_0=100\,{\rm kPa}$, sound velocity in the liquid $c=1500\,{\rm m\,s^{-1}}$ and a driving frequency of $\omega=2\pi\cdot 20\,{\rm kHz}$†.

For bubbles whose equilibrium radius R_0 fulfils the condition $4\mu/\rho c\ll R_0\ll c/\omega=\lambda/2\pi$, and small amplitudes $P_{\rm a}\ll p_0$ of the external sound-field, a linearization

† For the Gilmore model (Gilmore 1952) qualitatively the same results have been obtained.

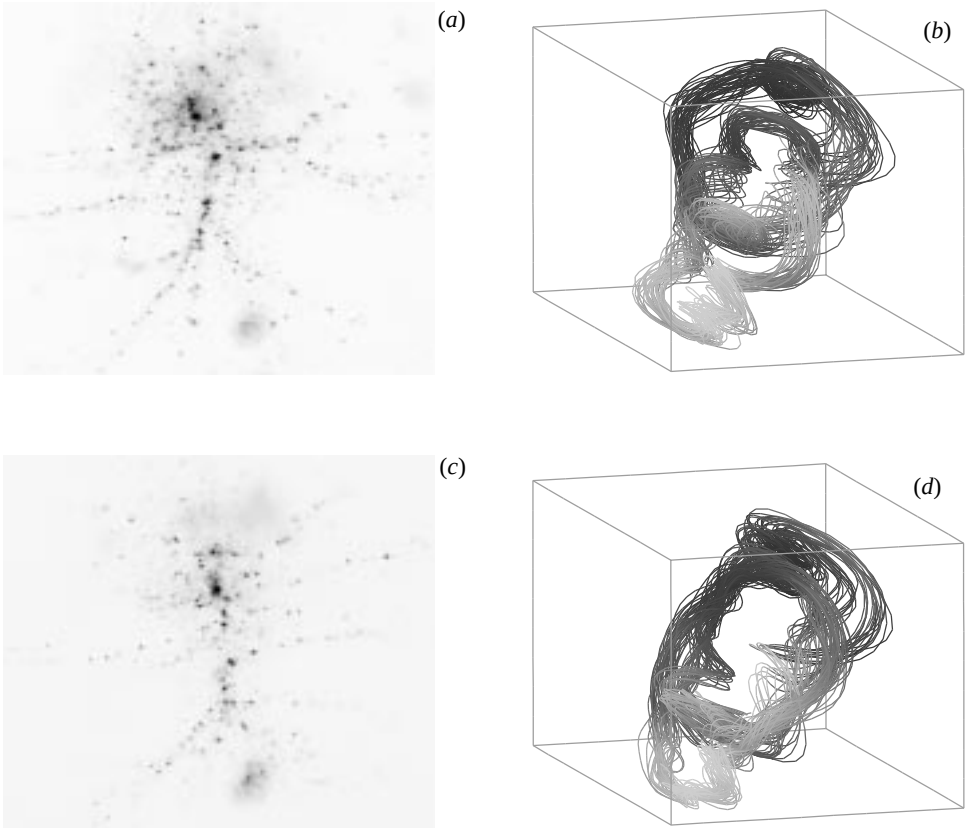

Figure 3. (*a*) and (*c*) show consecutive snapshots of the bubble structure that are separated in time by a few seconds. The pictures have been black/white inverted for better visibility. (*b*) and (*d*) show corresponding three-dimensional attractor reconstructions from the hydrophone signal.

of the Keller–Miksis model with $R(t) = R_0 + R'(t)$ yields the equation

$$\ddot{R}' + \alpha\dot{R}' + \omega_0^2 R' = -\frac{P_\mathrm{a}}{\rho R_0}\cos(\omega t), \tag{3.3}$$

where

$$\omega_0^2 = \frac{1}{\rho R_0^2}\left[3\kappa p_0 + \frac{2\sigma}{R_0}(3\kappa - 1)\right], \qquad \alpha = \frac{4\mu}{\rho R_0^2} + \frac{\omega_0^2 R_0}{c}. \tag{3.4}$$

As can be seen from equation (3.4), the role of ω_0 and R_0 can be exchanged: for fixed bubble size R_0, we can speak of a linear resonance frequency ω_0, and for fixed frequency ω, we can find a linear resonance bubble radius $R_\mathrm{r} = R_0$ via (3.4). The relationship is approximated (for normal air pressure and for water, neglecting σ) by the easily memorizable form $\nu_0 R_\mathrm{r} \approx 3\ \mathrm{ms}^{-1}$ with $\omega_0 = 2\pi\nu_0$.

(*b*) *Dynamics of acoustic waves in bubbly liquids*

A bubbly liquid may be considered a continuum (in an average sense) when bubble sizes and inter-bubble distances are small compared to the distances over which

the macroscopic quantities of the mixture change. On the basis of such assumptions, van Wijngaarden (1968) heuristically derived equations of motion for bubbly liquids that were confirmed by Caflish *et al.* (1985) using a more mathematically rigorous derivation (see also Nigmatulin 1991). These equations are valid for a weakly compressible fluid where the volume fraction of gas, α, is small, and they may be used to derive the following wave equation for the pressure p in the mixture (Commander & Prosperetti 1989):

$$\frac{1}{c^2}\frac{\partial^2 p}{\partial t^2} - \Delta p = 4\pi\rho \int_0^\infty \hat{R}_0^2 N(\boldsymbol{x}, \hat{R}_0)\ddot{R}\,\mathrm{d}\hat{R}_0, \tag{3.5}$$

where the speed of sound c and the density of the pure liquid ρ are assumed to be constant. $N(\boldsymbol{x}, \hat{R}_0)$ gives the probability density for finding a bubble with equilibrium radius $\hat{R}_0$ at the point $\boldsymbol{x}$. For a monodisperse mixture of bubbles of size R_0 we obtain with $N(\boldsymbol{x}, \hat{R}_0) = N_0 n(\boldsymbol{x})\delta(\hat{R}_0 - R_0)$

$$\frac{1}{c^2}\frac{\partial^2 p}{\partial t^2} - \Delta p = 4\pi\rho N_0 n R_0^2 \ddot{R} = \frac{\omega_0^2}{c^2}\rho R_0 \epsilon n \ddot{R}, \tag{3.6}$$

with

$$\epsilon = \frac{c^2\rho}{\kappa p_0}\frac{4\pi}{3}R_0^3 N_0, \qquad \omega_0^2 = \frac{3\kappa p_0}{\rho R_0^2}. \tag{3.7}$$

N_0 is a characteristic concentration constant, $n = n(\boldsymbol{x})$ gives the normalized dimensionless spatial distribution of the bubbles, ϵ is a small parameter, and ω_0 equals the linear resonance frequency of the bubbles (3.4) if surface tension is neglected.

(*c*) *Bjerknes forces*

A body in an inhomogeneous pressure field experiences a force in the direction of lower pressure. In a gravitational environment, for instance, this leads to the buoyancy force (which is neglected throughout this article). For bubbles in a sound field, additional forces appear due to the oscillations of the pressure gradient and the bubble volume. If the bubble is small compared to the typical spatial scale of pressure variations (the wavelength $\lambda = 2\pi c/\omega$), we can write this force known as the Bjerknes force (Bjerknes 1906; Young 1989; Leighton 1994)

$$\boldsymbol{F}_\mathrm{B} = -\langle V(t)\nabla p(t)\rangle_t, \tag{3.8}$$

where $V = \frac{4}{3}\pi R^3$ is the bubble volume, $\nabla p(t)$ denotes the gradient of the pressure at the bubble's position, and $\langle\cdot\rangle_t$ indicates a time average.

In general, the Bjerknes forces are separated into primary and secondary components, depending on the origin of the pressure gradient. Primary Bjerknes forces relate to the gross incident sound field originally causing bubble oscillations. Secondary Bjerknes forces refer to the sound emitted from other bubbles, which is a secondary effect. The primary Bjerknes forces act relative to the externally imposed acoustic field, while the secondary Bjerknes forces act between bubbles.

The sign and magnitude of the forces depend very much on details of the bubble oscillation. In the following, we study Bjerknes forces occurring for strongly nonlinear oscillations and compare the results with approximations obtained for bubbles oscillating harmonically. The nonlinear bubble dynamics is simulated by numerically

integrating the Keller–Miksis model (3.1), and for the investigation of harmonic bubble oscillations we use equation (3.3).

The inhomogeneous solution of the linear ordinary differential equation (3.3) is given by $R'(t) = R'_A \cos(\omega t + \varphi)$ that is characterized by an amplitude $R'_A = R'_A(\omega, R_0)$ and a phase shift $\varphi = \varphi(\omega, R_0)$. The linearized model tells us that bubbles larger than linear resonance radius, R_r, oscillate in such a way that they have large volume at high pressure phases ($\varphi \in [0, \pi/2]$), and smaller bubbles have large volume during low pressure times ($\varphi \in [\pi/2, \pi]$).

The *primary Bjerknes force* acting on the harmonically oscillating bubble in a standing sound field $p(\boldsymbol{x}, t) = p_0 + P_\mathrm{a}(\boldsymbol{x}) \cos(\omega t)$, may be expressed as

$$\boldsymbol{F}_\mathrm{B1} = -\tfrac{1}{2} V_A \nabla P_\mathrm{a} \cos(\varphi), \tag{3.9}$$

where $V_A = 4\pi R_0^2 R'_A$ denotes the amplitude of the linear volume oscillation, which is phase shifted with respect to the pressure, $V(t) = V_0 + V_A \cos(\omega t + \varphi)$. With the phase considerations above, the following result is obtained: for bubbles smaller than the linear resonance radius, the force $\boldsymbol{F}_\mathrm{B1}$ acts in direction towards the pressure antinode ($\cos(\varphi) < 0$), while larger bubbles ($\cos(\varphi) > 0$) are attracted by the pressure node (Leighton 1994). However, this well-known result is not strictly valid for nonlinear bubble oscillations. Let us consider the vicinity of a pressure antinode where ALFs appear. Figure 4*a* shows that bubbles of decreasing size are repelled for increasing driving amplitude. The reason is that the relative phase between exciting pressure and bubble response is affected by the amplitude of oscillation. The occurrence of nonlinear resonances leads to a certain zigzag course of the border between attractive and repulsive primary Bjerknes force. Near the centre of the diagram, chaotic bubble oscillations and coexisting attractors cause a complicated pattern that is not fully resolved. Note that above a pressure amplitude of about 180 kPa, only bubbles of the order of micrometres in radius are still attracted by the antinode, which is in striking contrast to the linear theory (Akhatov *et al*. 1997).

Similar strong effects of nonlinear oscillations have been found for the *secondary Bjerknes forces* (Oguz & Prosperetti 1990; Mettin *et al*. 1997). The force of an oscillating bubble '1' on a neighbouring bubble '2' is given to some approximation by

$$\boldsymbol{F}_\mathrm{B2} = -\frac{\rho}{4\pi} \langle \dot{V}_1 \dot{V}_2 \rangle \frac{\boldsymbol{x}_2 - \boldsymbol{x}_1}{\|\boldsymbol{x}_2 - \boldsymbol{x}_1\|^3}, \tag{3.10}$$

where $\boldsymbol{x}_1$ and $\boldsymbol{x}_2$ denote the locations of the interacting bubbles. For harmonic bubble oscillations we obtain

$$\boldsymbol{F}_\mathrm{B2} = -\frac{\rho\omega^2}{8\pi} V_{1\mathrm{A}} V_{2\mathrm{A}} \cos(\varphi_1 - \varphi_2) \frac{\boldsymbol{x}_2 - \boldsymbol{x}_1}{\|\boldsymbol{x}_2 - \boldsymbol{x}_1\|^3}, \tag{3.11}$$

where $V_{1\mathrm{A}}$, $V_{2\mathrm{A}}$ and φ_1, φ_2 are the amplitudes and the phases of the volume oscillations $V_i(t) = V_{i0} + V_{iA} \cos(\omega t + \varphi_i)$ $(i = 1, 2)$, respectively. According to this result, a bubble smaller than the linear resonance radius and a larger bubble repel each other, while pairs of smaller or larger bubbles experience an attracting secondary Bjerknes force. The inclusion of the nonlinearity, of a coupling of the oscillations, or of shape distortions, for instance, can lead to considerable change of this situation. We briefly outline the influence of strong nonlinear oscillation in equation (3.11) on small spherical bubbles (Mettin *et al*. 1997). It is found that the magnitude of the

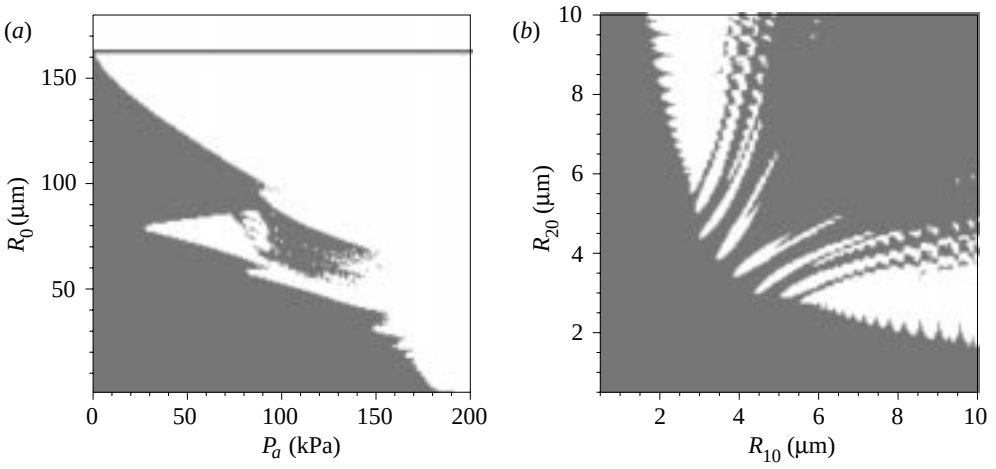

Figure 4. (*a*) Effect of the primary Bjerknes force near a pressure antinode ($\omega = 2\pi \cdot 20$ kHz). The dark regions in the plane of pressure amplitude, P_a, and bubble equilibrium radius, R_0, indicate attraction, the bright regions repulsion. The linear resonance radius (*ca.* 163 μm) is indicated by the dark horizontal line at $R_0 = 162$ μm. (*b*) Secondary Bjerknes forces between two neighbouring bubbles in the sound field ($P_a = 112$ kPa, $\omega = 2\pi \cdot 20$ kHz). The axes denote the equilibrium radii: the dark area indicates mutual attraction; the bright area mutual repulsion.

secondary Bjerknes force increases by orders of magnitude in comparison to linear theory, and that unforeseen mutual repulsion of bubbles may occur. A depiction in the R_{10}–R_{20}-plane is given by figure 4*b*. For fixed driving amplitude and frequency, the attraction and repulsion between bubbles is coded by dark and bright areas, respectively. The bubble radii below 10 μm are chosen because of their supposed relevance in the cavitation structures (see below).

These forces between oscillating bubbles may be further modified by the presence of additional neighbours, the motion of the bubbles relative to the liquid, or a time delay of the mutual action due to a finite sound speed. These effects are the subject of ongoing and future investigations.

(*d*) *Nucleation, growth, coalescence and destruction of bubbles*

There exist several mechanisms by which the bubbles in acoustic cavitation can be created (see, for example, Brennen 1995). All of them may play a role in typical structure-formation experiments. In particular, nucleation from the resonator wall and from contaminating tiny solid particles as well as from submerged microbubbles seems to be important. Microscopic voids of gas or vapour usually dissolve because of the surface tension of the liquid, but they can be stabilized against dissolution by surface active molecules, or by being embedded in particle crevices. Generally, microscopic sources of cavitation bubbles are termed cavitation nuclei.

There are only sparse measurements with respect to the bubble sizes participating in cavitation streamers. A recent study employing holographic high-speed cinematography (Billo 1997) reports bubble diameter distributions that peak between 30 and 150 μm in the expanded bubble-oscillation phase. Using typical parameter values of that experiment for pressure amplitude and frequency, the equilibrium radii of the bubbles can be calculated back to range between 1 and 10 μm. Such small values are

not significantly different from the data for general cavitation nuclei sizes (Brennen 1995).

In the presence of the sound field, microbubbles may expand to many times their equilibrium size during the low-pressure phase. In addition, they may grow slowly over many cycles of acoustic forcing by the influx of dissolved gas in the liquid in a process called 'rectified diffusion' (Young 1989; Leighton 1994). Bubbles that grow to many times their equilibrium sizes become susceptible to surface instabilities (Plesset 1954; Strube 1971; Prosperetti 1977) and may break up. The remnants of the destroyed bubbles consist of smaller bubbles and microbubbles that either dissolve or function as cavitation nuclei. The critical bubble size for break up is a decreasing function of the driving pressure amplitude, suggesting again that micron-sized bubble populations dominate in the high acoustic pressure fields.

In addition, there is a hydrodynamic effect of a fast-moving oscillating bubble on the liquid that is difficult to take into account. We suspect that the inwards streaming bubbles trigger a flow of liquid in the same direction, leaving the space between the filaments for outflowing liquid. Furthermore, a preferred (hydrodynamically supported) bubble nucleation in the wake of a streaming bubble might be possible. Such an effect would contribute to a stabilization of existing filament patterns.

(*e*) *Added mass and drag force*

A moving bubble generates a certain inertia and experiences a resistive friction force from the viscosity of the fluid. The inertia stems only partly from the mass of the gas inside the bubble; a much larger share is due to the inertia of the liquid streaming around it. This *added mass* for a rigid, spherical body amounts to half of the mass of the displaced liquid, and thus the gas mass is usually neglected. For an oscillating bubble, however, the determination of the effective added mass becomes more complicated, and difficulties increase if non-spherical shapes are considered.

The situation is similar for the viscous drag force. Only for simple conditions like a steady flow of low Reynolds number around a rigid sphere can the drag be predicted accurately. Higher streaming velocities, oscillating or non-spherical body shapes render an analytical treatment much more involved. Closer investigation of the hydrodynamic force on a moving oscillating spherical bubble reveals, for instance, that the bubble-wall velocity contributes to the added mass, and that the wake behind the bubble leads to the Basset force, a memory term adding to the viscous drag force (see, for example, Brennen 1995; Nigmatulin 1991).

Experimental investigations of these phenomena are not very numerous and, therefore, we refer to the Stokes friction force for low Reynolds number in the continuum model, and to experimental data based on rising non-oscillating bubbles in the particle approach.

4. Continuum description

In this section, a continuum model is presented for the interaction between the sound field and the bubble distribution. It consists of three coupled partial differential equations for the sound-field amplitude, the bubble velocity and the bubble density. A more detailed description of this model can be found in Akhatov *et al*. (1996). A linear stability analysis based on this model shows that a homogeneous monodisperse distribution of bubbles is unstable in the presence of an acoustic wave.

(*a*) *Sound-field amplitude*

When considering the spatio-temporal dynamics of bubbly liquids, one has to include the relative motion between the two phases. However, the process of redistribution of bubbles is a slow process on a time-scale much larger than the period of the acoustic field. This is confirmed by the experiments described in § 2. Therefore, assuming only weak pressure disturbances, equation (3.6) should remain valid if we allow for a slow time-scale variation of the number density $n(\boldsymbol{x})$. In the absence of bubbles ($N_0 = 0$), a plane acoustic wave propagating along the z-axis is an exact solution of equation (3.6):

$$p = p_0 + \frac{1}{2}\left\{W_0 \exp\left[\mathrm{i}\omega\left(t - \frac{z}{c}\right)\right] + \text{c.c.}\right\}, \tag{4.1}$$

where W_0 is the constant complex wave amplitude and 'c.c.' denotes the complex conjugate. Let us consider small perturbations of W_0 perpendicular to the direction of propagation. To account for a slow redistribution of bubbles, we approximate the solution of equation (3.6) in the form

$$p = p_0 + \frac{1}{2}\left\{W(\epsilon t, \sqrt{\epsilon}x, \sqrt{\epsilon}y) \exp\left[\mathrm{i}\omega\left(t - \frac{z}{c}\right)\right] + \text{c.c.}\right\}, \tag{4.2}$$

where ϵ, as taken from (3.7), is small for typical values of the parameters†. In order to obtain an analytic expression for the right-hand side of equation (3.6), we consider bubble oscillations of small amplitude that are governed by the linearized equation (3.3). Since W is a quantity slowly varying in time and space, the solution to equation (3.3) can be approximated by

$$R' = -\frac{1}{2}\frac{1}{\rho R_0(\omega_0^2 - \omega^2)}\left\{W(\epsilon t, \sqrt{\epsilon}x, \sqrt{\epsilon}y) \exp\left[\mathrm{i}\omega\left(t - \frac{z}{c}\right)\right] + \text{c.c.}\right\}, \tag{4.3}$$

where damping terms have been neglected ($\alpha = 0$). Substituting equations (4.2) and (4.3) into equation (3.6) and neglecting terms $O(\epsilon^2)$, yields, in the low-frequency limit $\omega \ll \omega_0$, a partial differential equation for the complex wave amplitude,

$$\mathrm{i}\frac{\partial w}{\partial \xi} = \frac{\partial^2 w}{\partial \eta^2} + \frac{\partial^2 w}{\partial \zeta^2} + nw, \tag{4.4}$$

where dimensionless variables ξ, η, ζ and w have been introduced with

$$\xi = \tfrac{1}{2}\omega\epsilon t, \qquad \eta = \frac{\omega}{c}\sqrt{\epsilon}x, \qquad \zeta = \frac{\omega}{c}\sqrt{\epsilon}y, \qquad w = \frac{W}{W_0}. \tag{4.5}$$

Equation (4.4) is essentially a nonlinear Schrödinger equation with the potential being replaced by the number density n.

(*b*) *Bubble velocity*

All bubbles of a volume V experience the primary Bjerknes force (3.8). From (4.2) and (4.3) we derive (Akhatov *et al.* 1996)

$$\boldsymbol{F}_\mathrm{B} = \gamma_1\left(\frac{\partial(|W|^2)}{\partial \eta}, \frac{\partial(|W|^2)}{\partial \zeta}, 0\right), \qquad \gamma_1 = \frac{3V_0}{4\rho R_0^2(\omega_0^2 - \omega^2)}\frac{\omega}{c}\sqrt{\epsilon}. \tag{4.6}$$

† For example, $\epsilon \sim 0.04$ for $c \sim 10^3$ m s^{-1}, $\rho \sim 10^3$ kg m^{-3}, $\kappa \sim 1$, $p_0 \sim 10^5$ N m^{-2}, $R_0 \sim 10^{-5}$ m and $N_0 \sim 10^9$ m^{-3}.

To account for interactions between bubbles and liquid, we include the Stokes friction force $\boldsymbol{F}_{\mathrm{S}}$ and the added mass force $\boldsymbol{F}_{\mathrm{M}}$ in their simplest form:

$$\boldsymbol{F}_{\mathrm{S}} = -6\pi\mu_1 R_0 \boldsymbol{U}, \tag{4.7}$$

$$\boldsymbol{F}_{\mathrm{M}} = -\tfrac{1}{2}\rho V_0 \frac{\partial \boldsymbol{U}}{\partial t}. \tag{4.8}$$

Here, $\boldsymbol{U}$ denotes the slow average drift velocity of the bubbles. We neglect the mass of the gas inside the bubble, secondary Bjerknes forces and buoyancy forces to write:

$$\boldsymbol{F}_{\mathrm{B}} + \boldsymbol{F}_{\mathrm{S}} + \boldsymbol{F}_{\mathrm{M}} = \boldsymbol{0}. \tag{4.9}$$

This yields an equation of motion for the slow drift of bubbles in the following form:

$$\tau_2 \frac{\partial \boldsymbol{u}}{\partial \xi} + \boldsymbol{u} = \gamma \nabla_{\eta\zeta}(|w|^2), \tag{4.10}$$

where we introduce the quantities

$$\boldsymbol{u} = \frac{\boldsymbol{U}}{U_*}, \qquad U_* = \tfrac{1}{2}c\sqrt{\epsilon}, \qquad \gamma = \frac{\gamma_1}{6\pi\mu_1 R_0}\frac{W_0^2}{U_*}, \qquad \tau_2 = \frac{\rho V_0}{24\pi\mu_1 R_0}\omega\epsilon. \tag{4.11}$$

(c) *Bubble density*

When considering the slow evolution of the bubble concentration, one has to take into account that bubbles usually dissolve after some time without an acoustic field. Therefore, we assume an exponential decay of the number density in the absence of a sound field. We also take into account the generation of bubbles due to the acoustic driving. For small pressure amplitudes, the energy flow supporting the bubble generation during one period is proportional to the sound-field intensity (Nigmatulin 1991). High intensities lead to a saturation value N_∞ of the bubble density due to the limited amount of dissolved gas in the liquid. These effects are included heuristically in the continuity equation for the number density:

$$\left.\begin{aligned} \frac{\partial n}{\partial \xi} + \nabla_{\eta\zeta}(n\boldsymbol{u}) &= -\frac{n - f(|w|^2)}{\tau_1}, \\ f(|w|^2) &= A_\infty^2[1 - \exp(-|w|^2/A_\infty^2)]. \end{aligned}\right\} \tag{4.12}$$

τ_1 is a dimensionless characteristic time of dissolution and the function $f(|w|^2)$ describes the saturation during the process of bubble generation with

$$\lim_{|w|\to\infty} f(|w|^2) = A_\infty^2 = N_\infty/N_0.$$

(d) *Stability analysis*

An analytic solution of the continuum model (4.4), (4.10) and (4.12) is given by

$$A = A_0 = \text{const.}, \qquad n = f(A_0^2), \qquad \Theta = -f(A_0^2)\xi, \qquad u_x = 0, \qquad u_y = 0, \tag{4.13}$$

where the amplitude A and the phase Θ are defined by

$$w = A(\xi,\eta,\zeta)\exp(\mathrm{i}\Theta(\xi,\eta,\zeta)). \tag{4.14}$$

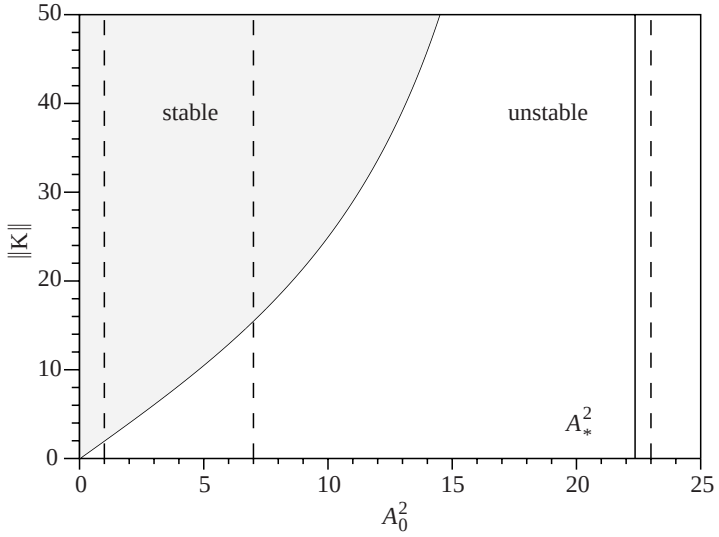

Figure 5. Stability diagram for periodic perturbations of the homogeneous solution (4.13) of the continuum model ($\tau_1 = 1$, $\tau_2 = 0.1$, $\gamma = 0.001$, $A_\infty \to \infty$). Perturbations with amplitudes $A_0 < A_*$ and sufficiently large wavenumbers $\|\boldsymbol{K}\| = [k_x^2 + k_y^2]^{1/2}$ decay. The homogeneous solution is unstable for long wavelengths (i.e. $\|\boldsymbol{K}\|$ small) or amplitudes A_0 above the threshold A_* indicated by the vertical solid line. The dashed lines give three values of A_0 that are used for figure 6.

Equations (4.13) and (4.14) describe a monochromatic wave in a mixture with a homogeneous and stationary bubble distribution. The evolution of small periodic perturbations of this uniform solution,

$$\begin{pmatrix} \tilde{A} \\ \tilde{\Theta} \\ \tilde{n} \\ \tilde{u}_x \\ \tilde{u}_y \end{pmatrix} = \begin{pmatrix} \hat{A} \\ \hat{\Theta} \\ \hat{n} \\ \hat{u}_x \\ \hat{u}_y \end{pmatrix} \exp(\sigma\xi + \mathrm{i}K_x\eta + \mathrm{i}K_y\zeta), \tag{4.15}$$

is described by a linearization of (4.4), (4.10) and (4.12). The stability of the uniform solution depends on the sign of the real part of the growth-rate coefficient σ that turns out to be positive for long-wavelength perturbations as is shown in the stability diagram in figure 5. For A_0 larger than a threshold value A_*, the uniform solution is unstable for all wavenumbers $\boldsymbol{K} = (K_x, K_y)$. Amplitudes A_0 smaller than A_* lead to an effective pattern selection, since, in this case, perturbations with short wavelength are decreasing. The remaining long-wavelength instability may be interpreted as the origin of structure formation, where, additionally, different growth rates of the unstable modes have to be taken into account. In figure 6, these growth rates are shown as a function of $\|\boldsymbol{K}\|$ for three values of the amplitude A_0.

(*e*) *Numerical simulations*

In this section we present numerical simulations based on the model equations (4.4), (4.10), (4.12) for a one-dimensional wavefront propagating along the z-axis in

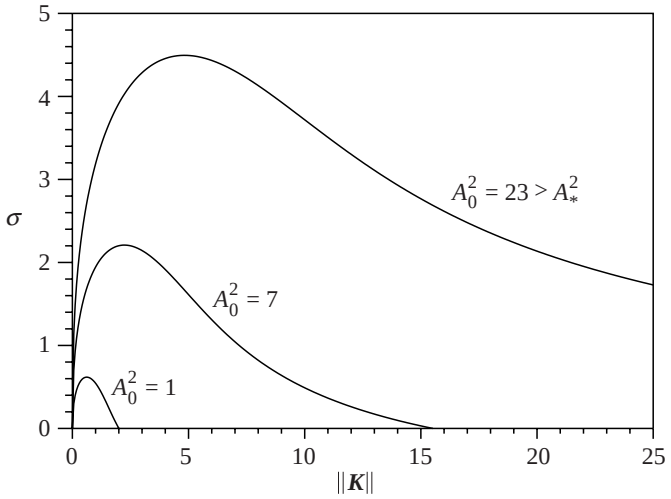

Figure 6. Growth rates σ of (unstable) modes versus wavenumber $\|\boldsymbol{K}\|$ for $A_0 = 1, 7, 23$ and $\tau_1 = 1$, $\tau_2 = 0.1$, $\gamma = 0.001$, $A_\infty \to \infty$ (compare with figure 5). If the wavenumber $\|\boldsymbol{K}\|$ of the perturbation is sufficiently small, also higher spatial harmonics with $2\|\boldsymbol{K}\|$, $3\|\boldsymbol{K}\|$, etc., may grow due to the long-wavelength instability.

a 'channel' of width $L = 2\pi/k$. The boundary conditions are given by

$$\frac{\partial w}{\partial \eta}(\xi, 0) = 0 = \frac{\partial w}{\partial \eta}(\xi, L),$$
$$u(\xi, 0) = 0 = u(\xi, L),$$
$$n(\xi, 0) = 0 = n(\xi, L),$$

and the following initial conditions are used:

$$w(0, \eta) = w_0[1 + \tfrac{1}{2} w_1[1 - \cos(\eta)]], \quad \eta \in [0, L],$$
$$u(0, \eta) = 0,$$
$$n(0, \eta) = |w(0, \eta)|^2,$$

with $w_0 = 1$ and $w_1 = 0.05$. A typical transient following the initial (linear) long-wavelength instability is shown in figure 7.

The instability leads to self-focusing of the acoustic wave and self-concentration of bubbles. Bubbles are driven to regions of higher sound-field amplitude that causes a decrease of sound velocity. Therefore the amplitude increases again until nonlinear effects lead to a saturation of the self-concentration effect. As τ_1 describes the characteristic lifetime of bubbles, an increase of τ_1 leads to more strongly damped oscillatory transients that converge to a quasi-asymptotic solution.

Due to nonlinearity, higher unstable modes can be excited. Examples with two unstable modes are given in figure 8, where nonlinear-mode competition occurs between the first ($k = 0.6$) and the second mode ($k = 1.2$).

Finally, two limitations of the present model need to be addressed. The strong increase of the local bubble concentration, as shown in figures 7 and 8, may violate the assumptions made for the derivation of the model. The second point concerns also the case of high bubble concentrations and high sound-field amplitudes, where

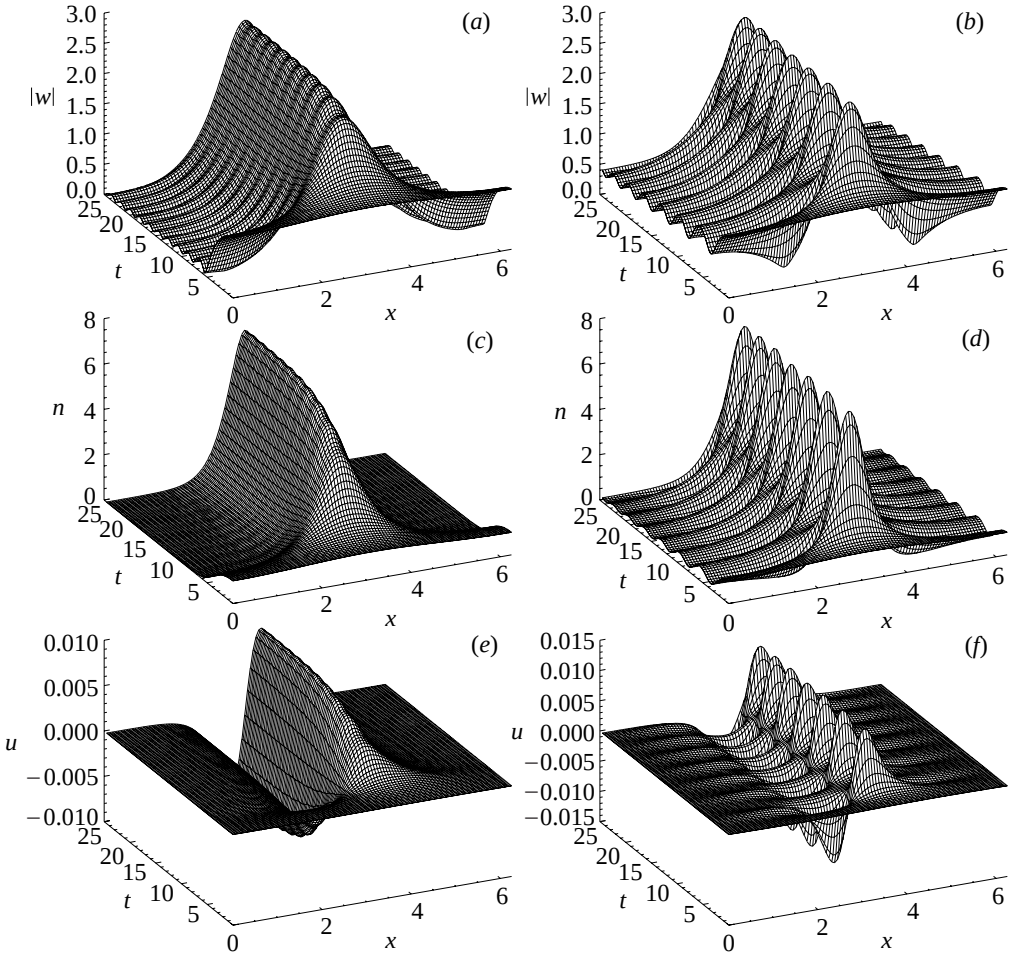

Figure 7. Spatio-temporal evolution of the magnitude of (*a*), (*b*) the sound-field amplitude $|w|$, (*c*), (*d*) the bubble density n and (*e*), (*f*) the bubble velocities u for $\tau_1 = 1$, $\tau_2 = 0.1$, $\gamma = 0.001$, $A_\infty \to \infty$, $K = 1$ ((*a*), (*c*), (*e*)); and $\tau_1 = 0.01$, $\tau_2 = 0.01$, $\gamma = 0.001$, $A_\infty \to \infty$, $K = 1$ ((*b*), (*d*), (*f*)).

one has to account for direct bubble–bubble interactions (secondary Bjerknes force) that are not yet included in the present model.

5. Particle model

In this model, the individual bubbles in the liquid are treated as moving particles. This idea is obvious if one is interested in the motion of only a few bubbles, and here we try to extend it to a complex multibubble system. Pioneering work in this direction by Hinsch (1976) has shown good agreement with experiments in the linear oscillation regime†.

† Static bubble patterns have been simulated using a diffusion-limited aggregation scheme (Parlitz *et al*. 1995).

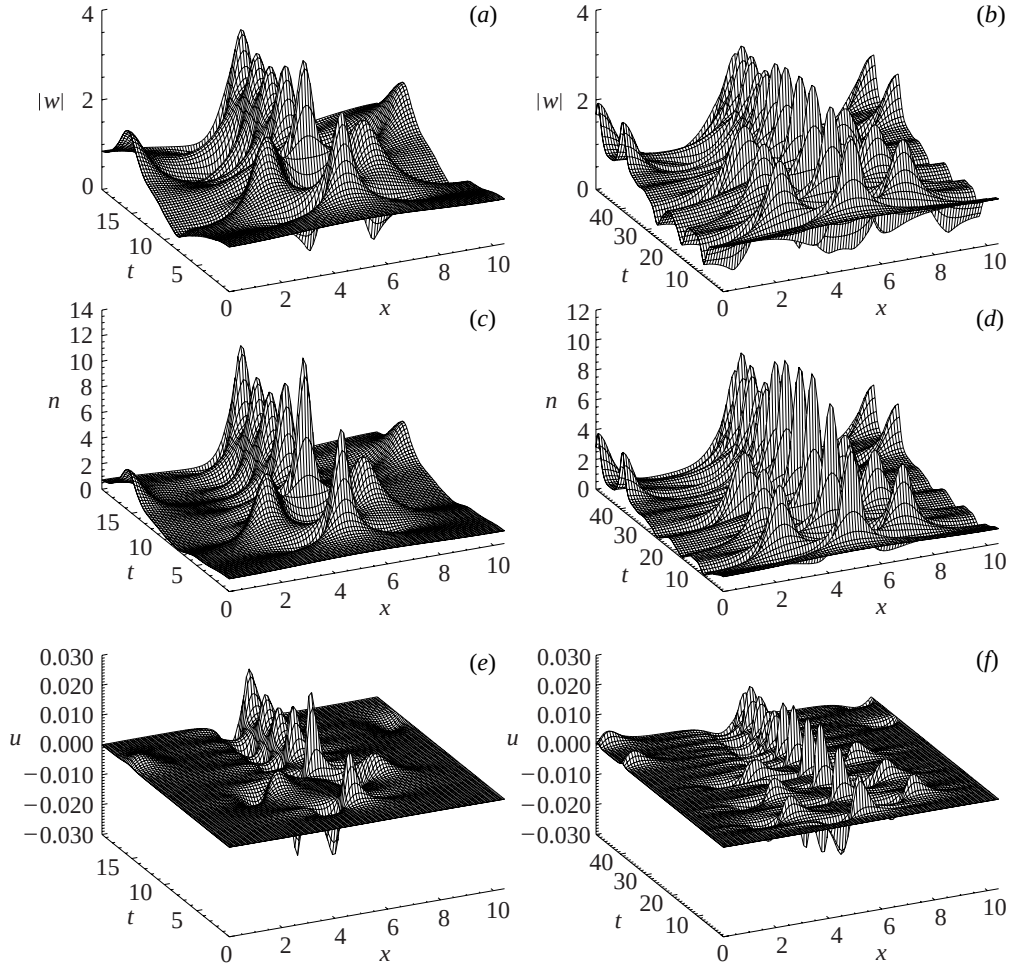

Figure 8. Spatio-temporal evolution of the magnitude of (*a*), (*b*) the sound-field amplitude $|w|$, (*c*), (*d*) the bubble density n and (*e*), (*f*) the bubble velocities u for $\tau_1 = 0.001$, $\tau_2 = 0.01$, $\gamma = 0.001$, $A_\infty \to \infty$, $K = 0.6$ ((*a*), (*c*), (*e*)); and $\tau_1 = 0.005$, $\tau_2 = 0.01$, $\gamma = 0.001$, $A_\infty \to \infty$, $K = 0.6$ ((*b*), (*d*), (*f*)).

The following forces acting on each bubble are considered: added mass force $\boldsymbol{F}_{\mathrm{M}}$; primary Bjerknes force $\boldsymbol{F}_{\mathrm{B1}}$; secondary Bjerknes force $\boldsymbol{F}_{\mathrm{B2}}$; and a drag force $\boldsymbol{F}_{\mathrm{D}}$. In contrast to the continuum approach, the influence of the bubble density on the exciting sound field is neglected. Further, we assume a stationary non-streaming liquid in a resonator containing a standing wave $p_{\mathrm{a}}(\boldsymbol{x};t) = P_{\mathrm{a}}(\boldsymbol{x})\cos(\omega t)$. The model is limited to spherical bubbles of the same equilibrium size R_0. However, we allow for strongly nonlinear radial bubble oscillations, which is an essential point. The time-varying radii $R(t)$ are computed by the Keller–Miksis model, equations (3.1) and (3.2), for the local driving pressure at the bubbles' positions. We consider slowly moving bubbles, i.e. bubbles do not encounter different sound-field amplitudes during one radial oscillation period (which is assumed equal to the sound-field oscillation period $T = 2\pi/\omega$ for all bubbles). Then, the forces are determined as follows, involv-

ing time averaging over T:

$$\boldsymbol{F}^i_{\mathrm{M}} = \tfrac{1}{2}\rho\langle V_i(t)\rangle_T \dot{\boldsymbol{v}}_i, \tag{5.1}$$

$$\boldsymbol{F}^i_{\mathrm{B1}} = -\langle \nabla p_{\mathrm{a}}(\boldsymbol{x}_i; t) V_i(t)\rangle_T, \tag{5.2}$$

$$\boldsymbol{F}^i_{\mathrm{B2}} = \sum_{j\neq i} \frac{\rho}{4\pi}\langle \dot{V}_i(t)\dot{V}_j(t)\rangle_T \frac{\boldsymbol{d}_{ij}}{\|\boldsymbol{d}_{ij}\|^3} \approx f^i_{\mathrm{B2}} \sum_{j\neq i} \frac{\boldsymbol{d}_{ij}}{\|\boldsymbol{d}_{ij}\|^3}, \qquad f^i_{\mathrm{B2}} = \frac{\rho}{4\pi}\langle \dot{V}_i^2(t)\rangle_T, \tag{5.3}$$

$$\boldsymbol{F}^i_{\mathrm{D}} = -(\beta_1\langle R(t)\rangle_T + \beta_2\langle R(t)\rangle_T^2 \|\boldsymbol{v}_i\|)\boldsymbol{v}_i. \tag{5.4}$$

Here, i indexes the bubbles with positions $\boldsymbol{x}_i$, velocities $\boldsymbol{v}_i$, and volumes V_i. $\boldsymbol{d}_{ij} = \boldsymbol{x}_j - \boldsymbol{x}_i$ is the vector from bubble i in direction to bubble j. The drag force $\boldsymbol{F}_{\mathrm{D}}$ is fitted to an experimentally based formula from Crum (1975) leading to the coefficients $\beta_1 = 0.015\ \mathrm{N\,s\,m^{-2}}$, $\beta_2 = 4000\ \mathrm{N\,s^2\,m^{-3}}$. The equations of motion

$$\boldsymbol{F}^i_{\mathrm{M}} = \boldsymbol{F}^i_{\mathrm{B1}} + \boldsymbol{F}^i_{\mathrm{B2}} + \boldsymbol{F}^i_{\mathrm{D}},$$

are solved by a semi-implicit Euler method for N bubbles.

According to the standing pressure wave in the container, the driving amplitude varies in space. Due to this sound-field variation, $R(t)$ and the resulting forces can change dramatically when a bubble moves to a different position. To keep the computations simple and fast, we introduced the approximation of equal bubble volumes for the summation of $\boldsymbol{F}_{\mathrm{B2}}$ in equation (5.3). Additionally, the time-averaged values in equation (5.1)–(5.4) are tabulated on a grid in space, and linear interpolation is used between the grid points. Figure 9 illustrates the strong quantitative and even qualitative variation of the primary and secondary Bjerknes forces for increasing pressure amplitude. The calculations have been done for a cubic resonator (edge length $a = 6\ \mathrm{cm}$, $\omega = 2\pi \cdot 21.66\ \mathrm{kHz}$ according to the (111) mode) and the fixed bubble size of $R_0 = 5\ \mu\mathrm{m}$ to come close to the described experiment (figure 2). The first component of the primary Bjerknes force, $F_{\mathrm{B1},1}$, shows increasing attraction (negative values) towards the pressure antinode (the origin) for an increasing driving pressure up to 160 kPa (the negative values associated with 100 kPa are very close to zero in this scaling). The sign of the force near the origin changes, however, when the amplitude is further increased up to 190 kPa: the antinode becomes repulsive for the bubble size considered. Since the force is still attractive in the outer regions of the standing wave, a stable equilibrium surface forms around the antinode. This evolution is accompanied by an increase of the secondary Bjerknes forces by orders of magnitude.

In the model, creation of bubbles takes place near some randomly chosen off-centre sites. This is similar to the experimental observation of bubble occurrence. Coalescence is modelled by a certain chance of annihilation after each time-step if another bubble is located closer than $2\langle R(t)\rangle_T$. If a bubble vanishes, a new one appears at a creation site. Thus, the total number N of bubbles is kept constant.

In figure 10 we compare typical results from the model with structures obtained in the experiment. The left-hand column of pictures corresponds to a central pressure amplitude of $P_{\mathrm{a}} = 130\ \mathrm{kPa}$, the right-hand column to $P_{\mathrm{a}} = 190\ \mathrm{kPa}$. The upper pictures show simulated bubble tracks in three dimensions, and the middle row depicts snapshots from the model projected onto two dimensions. The lower pictures present snapshots from the experiment that have been black/white inverted for better visibility. The parameters of the simulation correspond to figure 9 and strongly resemble

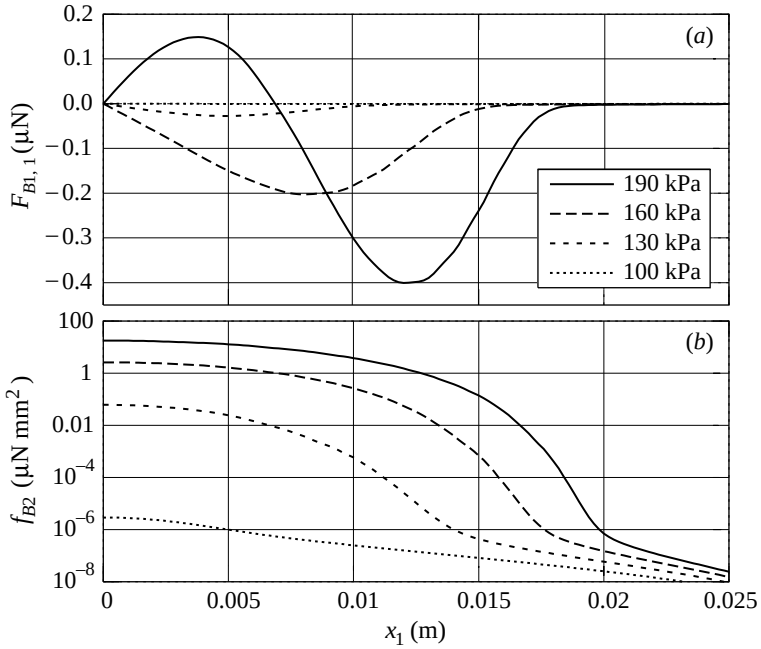

Figure 9. First component $F_{\mathrm{B1,1}}$ of the primary Bjerknes force (a) and secondary Bjerknes force coefficient f_{B2} (b) versus the first coordinate x_1 in a cubic resonator (see text; $x_2 = x_3 = 0$ in this picture). The maximum pressure amplitudes, P_{a}, ranges from 100 to 190 kPa. Positive values of $F_{\mathrm{B1,1}}$ indicate repulsion from the antinode. Note the logarithmic scaling in (b).

the experimental cubic resonator setup. Only the pressure amplitudes in the experiment might have differed slightly from the indicated values, and the cuvette has been chosen to be a little larger in the simulation to come close to the experimentally observed resonance frequency (in the range of 21 kHz). The simulated bubbles ($N = 150$, $R_0 = 5\,\mu\mathrm{m}$) originate at 20 fixed creation sites at 2 cm distance from the centre (the antinode). The bubble traces in the upper row of figure 10 cover a total simulation time of 0.4 s (130 kPa, left) and 0.1 s (190 kPa, right), respectively. These periods of time seem short enough to justify non-moving creation sites.

For the lower pressure, all simulated bubbles move more or less straight to the centre at velocities not exceeding 0.1 m s^{-1}. The geometry corresponds well with the physical features shown in the experimental snapshot although the nebulous centre is not captured by simulation.

The situation is different at a higher pressure amplitude. At 190 kPa bubbles move faster (up to 0.5 m s^{-1}) and cluster off-centre; the antinode is void, and the creation sites appear interconnected by shortcuts. The experiment indeed shows an analogous transition for increasing driving from one central cluster to many fast-drifting non-central smaller clusters. This scenario is difficult to image experimentally, but several small bubble clusters can be recognized as darker spots on the experimental snapshot (figure 10, bottom right). There are two effects contributing to this transition phenomenon: the antinode becomes repulsive for increasing pressure (compare figure 9a), and the secondary Bjerknes force increases by several orders of magnitude (see figure 9b). Therefore, the bubbles attract each other earlier when streaming from the outside and cluster near the stable equilibrium surface around the antinode.

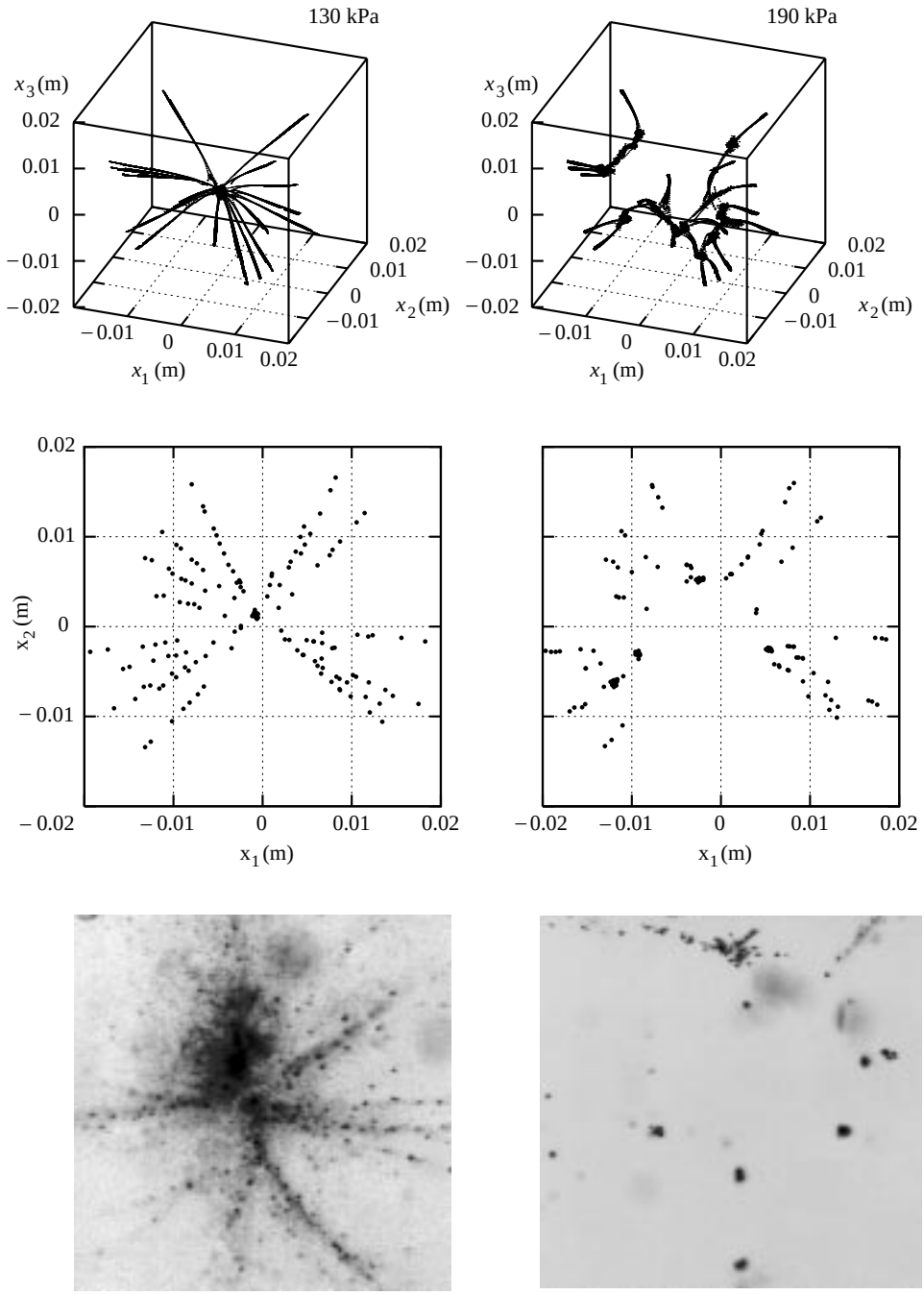

Figure 10. Typical examples of calculated bubble traces and snapshots compared to experimental structures. Left column: medium pressure amplitude (130 kPa); right column: high pressure amplitude (190 kPa). Top row: simulated bubble tracks (150 bubbles, originating from 20 fixed creation points). Middle row: snapshots from the simulations above. Bottom row: experimental photographs at approximately the same conditions and dimensions as in the simulations.

It is interesting to note that, if many bubbles were placed in the centre where f_{B2} is largest, their mutual attraction could possibly outrange the primary Bjerknes repulsion and lead to a bistability of central and off-centred clustering structure. Indeed, an intermittency on a time-scale of seconds between a populated and a void centre can be observed in our resonator experiments for certain parameters (without changing the pressure from the outside).

We suspect influence of the bubble distribution on the sound field, leading to effective pressure amplitude changes by impedance mismatch, or streaming of the liquid in the container, to be some of the possible underlying mechanisms inducing the transition between the multistable patterns.

The particle model with a few fixed bubble sources can apparently mimic the emergence of different types of structures in an acoustic resonator standing-wave experiment, as comparison of simulated and experimental patterns in figure 10 suggests. Furthermore, we have found that the simulated pattern of bubble tracks does not vary much within a certain range of the bubble quantity N if a sparse number of creation sites is used that stays fixed in time (a pattern transition might be modelled by variable creation sites, which is beyond the scope of this article). Therefore, one gets a good impression of the structure formation just by looking at the bubble traces. However, the full process is spatio-temporal and a three-dimensional (holographic) movie would be the most appropriate visualization tool.

We tried to use observed or estimated real-world mechanisms, dimensions and quantities in the particle model wherever possible, but this approach is still more of a cartoon than a one-to-one reproduction of the structure formation in acoustic cavitation. Variations of the bubble equilibrium size, shape oscillations (see, for example, Blake, this issue) and shedding of microbubbles, liquid streaming and exact treatment of very close bubbles have not been incorporated into the model (e.g. we have modified the secondary Bjerknes force law for very near distances in a heuristic manner to avoid unnatural divergencies in the simulation). This simple model can, however, already reproduce gross features of different pattern types. We therefore draw the main conclusion from our particle model studies that a strong spatial variation of Bjerknes forces, according to nonlinear spherical-bubble oscillations in a standing pressure wave, is consistent with experimental observations. This holds both qualitatively (the types of emerging patterns) and quantitatively (the involved time-scales and pressure amplitude values), and thus gives indication for a correct treatment of the Bjerknes forces of strongly oscillating bubbles (without a direct measurement).

6. Conclusion

Structure formation processes in cavitation bubble fields are a challenging physical phenomenon that is interesting from a fundamental point of view as well as for practical applications. Experimental observations indicate that complex dynamics on different time-scales and spatial scales occur that are mutually coupled. The collective behaviour observed on the macroscopic scale is a result of different processes on microscopic scales that have to be identified, investigated and described in order to derive theoretical models. Some of these building blocks have been briefly discussed in § 3. In §§ 4 and 5, two approaches for modelling the experimental observations have been presented: a continuum model and a particle model. In the continuum

model, the bubbly liquid is treated as a quasi-continuum and a set of coupled partial differential equations is derived describing the propagation of an acoustic wave and the time evolution of the bubble distribution. The main result is a long-wavelength instability of the homogeneous solution and a self-concentration effect of the bubble distribution. The particle approach presented in § 5 is based on the microscopic dynamics of individual oscillating bubbles that are treated as moving objects. Numerical simulations provide bubble patterns that are in good qualitative agreement with experimental results, although only some of the known physical mechanisms have been incorporated into the model as yet. Future improvements of the models should include, for example, provision for the (re)action of the bubble distribution on the sound field in the particle approach, or inclusion of secondary Bjerknes forces in the continuum approach. Furthermore, both models could be generalized to the case of bubbles of different equilibrium size. Another important aspect not yet included is the streaming of the liquid due to moving bubbles or nonlinear acoustic effects. Since the streamers in the 'acoustic Lichtenberg figures' are only sparsely populated, a combination of continuum and particle model might be a promising prospect for future work.

On the microscopic level, more detailed experimental investigations are necessary to improve our knowledge about acoustic streaming and fluid motion, drag and added mass forces of oscillating bubbles, Bjerknes forces acting on non-spherical bubbles or bubbles that are located very close together, and the interaction and synchronization of bubble oscillations. The lack of control and reproducibility of suitable events might be overcome by single-bubble experiments and laser-induced cavitation bubbles (Ohl *et al.*, this issue). Furthermore, combined optical and acoustic measurements may provide even more interesting details of this complex physical system.

We acknowledge support by the *Deutsche Forschungsgemeinschaft* (Graduiertenkolleg 'Strömungsinstabilitäten und Turbulenz') and the *Internationales Büro des BMBF* (contract RUS-133-1997). Furthermore, we thank our colleagues, in particular C.-D. Ohl, T. Kurz, R. Geisler and J. Allen for many stimulating discussions and careful reading of the manuscript.

References

Akhatov, I., Parlitz, U. & Lauterborn, W. 1996 *Phys. Rev.* E **54**, 4990–5003.

Akhatov, I., Mettin, R., Ohl, C.-D., Parlitz, U. & Lauterborn, W. 1997 *Phys. Rev.* E **55**, 3747–3750.

Billo, A. 1997 Holografische Partikelfeldanalyse am Beispiel Akustischer Lichtenberg-Figuren. PhD thesis, TH Darmstadt, Germany.

Bjerknes, V. F. K. 1906 *Fields of force.* New York: Columbia University Press.

Brennen, C. E. 1995 *Cavitation and bubble dynamics.* Oxford University Press.

Caflisch, R. E., Miksis, M. J., Papanicolaou, G. C. & Ting, L. 1985 *J. Fluid Mech.* **153**, 259–273.

Commander, K. W. & Prosperetti, A. 1989 *J. Acoust. Soc. Am.* **85**, 732–746.

Crum, L. A. 1975 *J. Acoust. Soc. Am.* **57**, 1363.

Flynn, H. G. 1964 Physics of acoustic cavitation. In *Physical acoustics* (ed. W. P. Mason), pp. 57–172. New York: Academic.

Gilmore, F. R. 1952 Report no. 26-4, Hydrodynamics Laboratory, California Institute of Technology, Pasadena, CA.

Hinsch, K. 1976 The dynamics of bubble fields in acoustic cavitation. In *Proc. 6th Int. Symp. on Nonlinear Acoustics, Moscow 1975* (ed. V. A. Akulichev *et al.*), pp. 26–34. Moscow University.

Keller, J. B. & Miksis, M. 1980 *J. Acoust. Soc. Am.* **68**, 628–633.
Lauterborn, W. & Holzfuss, J. 1991 *Int. J. Bifurcation Chaos* **1**, 13–26.
Lauterborn, W. & Parlitz, U. 1988 *J. Acoust. Soc. Am.* **84**, 1975–1993.
Lauterborn, W., Schmitz, E. & Judt, A. 1993 *Int. J. Bifurcation Chaos* **3**, 635–642.
Lauterborn, W., Kurz, T. & Parlitz, U. 1997 *Int. J. Bifurcation Chaos* **7**, 2003–2033.
Leighton, T. G. 1994 *The acoustic bubble*. London: Academic.
Mettin, R., Akhatov, I., Parlitz, U., Ohl, C.-D. & Lauterborn, W. 1997 *Phys. Rev.* E **56**, 2924–2931.
Neppiras, E. A. 1980 *Phys. Rep.* **61**, 159–251.
Nigmatulin, R. I. 1991 *Dynamics of multiphase media*, vol. 1, 2. New York: Hemisphere.
Oguz, H. N. & Prosperetti, A. 1990 *J. Fluid Mech.* **218**, 143–162.
Parlitz, U., Scheffczyk, C., Akhatov, I. & Lauterborn, W. 1995 *Int. J. Chaos, Solitons Fractals* **5**, 1881–1891.
Parlitz, U., Junge, L., Lauterborn, W. & Kocarev, L. 1996 *Phys. Rev.* E **54**, 2115–2117.
Plesset, M. S. 1954 *J. Appl. Phys.* **25**, 96–98.
Prosperetti, A. 1977 *Q. Appl. Math.* **34**, 339–352.
Rosenblum, M. G., Pikovsky, A. S. & Kurths, J. 1996 *Phys. Rev. Lett.* **76**, 1804.
Sauer, T., Yorke, J. A. & Casdagli, M. 1991 *J. Stat. Phys.* **65**, 579.
Strube, H. W. 1971 *Acustica* **25**, 289–303.
Takens, F. 1980 In *Dynamical systems and turbulence* (ed. D. A. Rand & L.-S. Young). Lecture Notes in Mathematics, vol. 898. New York: Springer.
van Wijngaarden, L. 1968 *J. Fluid. Mech.* **33**, 465–474.
Young, F. R. 1989 *Cavitation*. London: McGraw-Hill.

PHILOSOPHICAL TRANSACTIONS OF THE ROYAL SOCIETY A MATHEMATICAL, PHYSICAL & ENGINEERING SCIENCES